

Chapter 2

Rydberg Atoms

The Rydberg series was originally identified in the spectral lines of atomic hydrogen, where the binding energy W was found empirically to be related to the formula [87]

$$W = -\frac{\text{Ry}}{n^2}, \quad (2.1)$$

where Ry was a constant and n an integer. The theoretical underpinning for this scaling arrived with the Bohr model of the atom in 1913 [88], from which the Rydberg constant Ry could be derived in terms of fundamental constants

$$\text{Ry} = \frac{Z^2 e^4 m_e}{16\pi^2 \epsilon_0^2 \hbar^2}, \quad (2.2)$$

and n understood as the principal quantum number. From the Bohr model it was also possible to derive scaling laws for the atomic properties in terms of n , which were later verified from the full quantum mechanical treatment of Schrödinger in 1926 [89]. Table 2.1 summarises the scalings of the atomic properties for the low- ℓ Rydberg states. The most important property of the Rydberg states is the large orbital radius, and hence dipole moment, $\propto n^2$. The consequence of the incredibly large dipole moment is an exaggerated response to external fields and the ability to observe dipole-dipole interactions between atoms on the μm scale. Combining this with the relatively long

Property	n -scaling
Binding Energy W	n^{-2}
Orbital Radius	n^2
Energy difference of adjacent n states Δ	n^{-3}
Radiative Lifetime τ	n^{-3}

Table 2.1: Scaling laws for properties of the Rydberg states [91].

lifetimes, Rydberg atoms are well suited to applications in coherent quantum gates [90].

2.1 Alkali metal atom Rydberg states

Alkali metal atoms are similar to hydrogen, with a single valence electron orbiting a positively charged core which gives a $-1/r$ Coulomb potential at long range. However, the nucleus is surrounded by closed electron shells which screen the nuclear charge, giving the core a finite size. For the low orbital angular momentum states with $\ell \leq 3$, the electron orbit is extremely elliptic and can penetrate the closed electron shells. This exposes the valence electron to the unscreened nuclear charge, causing the core potential to deviate from the Coulombic potential at short range. The inner electrons can also be polarised by the valence electron. These two interactions with the core combine to increase the binding energy of the low- ℓ Rydberg states relative to the equivalent hydrogenic states. This difference in binding energy is parameterised using the quantum defects $\delta_{n\ell j}$

$$W = -\frac{\text{Ry}}{(n - \delta_{n\ell j})^2}, \quad (2.3)$$

where for rubidium the Rydberg constant is $\text{Ry} = 109736.605 \text{ cm}^{-1}$ [39]. The properties of the alkali metal Rydberg states are thus determined from the effective principal quantum number $n^* = n - \delta_{n\ell j}$.

The value of the quantum defects depends on the quantum numbers for the

Rydberg state of interest, where the S states have the largest defects as they have a significant core penetration. The quantum defects are determined empirically from spectroscopic measurements and can be calculated using

$$\delta_{n\ell j} = \delta_0 + \frac{\delta_2}{(n - \delta_0)^2} + \frac{\delta_4}{(n - \delta_0)^4} + \dots, \quad (2.4)$$

where $\delta_0, \delta_2 \dots$ are dependent upon ℓ and j . For rubidium, these have been measured on a cloud of cold atoms by the group of T. F. Gallagher and can be found in ref. [92] for the S, P and D states and ref. [93] for the F states. For $\ell > 3$ the quantum defects are zero, and the core potential is purely Coulombic. These are referred to as the hydrogenic states, which are degenerate for a given n .

2.2 Rydberg atom wavefunctions

The wavefunction for the valence electron is described by the Schrödinger equation, given in atomic units (a.u.) as

$$\left[-\frac{1}{2\mu} \nabla^2 + V(r) \right] \psi(r, \theta, \phi) = W \psi(r, \theta, \phi), \quad (2.5)$$

where μ is the reduced mass of the electron, r is the radial coordinate and $V(r)$ is the core potential. Since $V(r)$ has no angular dependence, the wavefunction is separable, giving $\psi(r, \theta, \phi) = R(r)Y_\ell^{m_\ell}(\theta, \phi)$, where $Y_\ell^{m_\ell}(\theta, \phi)$ is a spherical harmonic dependent upon the orbital angular momentum ℓ of the Rydberg state. Inserting this into eq. 2.5 gives the equation for the radial wavefunction of the electron

$$\left[-\frac{1}{2\mu} \left(\frac{d^2}{dr^2} + \frac{2}{r} \frac{d}{dr} \right) + \frac{\ell(\ell+1)}{2\mu r^2} + V(r) \right] R(r) = W R(r). \quad (2.6)$$

Model potential $V_C(r)$

To calculate the radial wavefunctions of the alkali metal atoms, it is necessary to use an ℓ -dependent core potential $V_C(r)$ to include the effects of core penetration and polarisation. This is done using a model potential given by [94]

$$V_C(r) = -\frac{Z_{n\ell}(r)}{r} - \frac{\alpha_c}{2r^4}(1 - e^{-(r/r_c)^6}). \quad (2.7)$$

The first term describes the Coulomb potential for a radial charge $Z_{n\ell}(r)$ to account for core penetration, where radial charge is defined as

$$Z_{n\ell}(r) = 1 + (Z - 1)e^{-a_1 r} - r(a_3 + a_4 r)e^{-a_2 r}. \quad (2.8)$$

The second term in eq. 2.7 describes the long range potential of the induced core polarisation on the valence electron. The strength of this effect is determined by the core polarisability α_c , which increases with the number of electrons in the core.

Values for the parameters a_{1-4} , r_c and α_c are taken from Marinescu *et al.* [94], where the authors fit this model for the core potential to the measured energies of the Rydberg states for each ℓ -series of the alkali metals.

In addition to the core potential, the spin-orbit potential $V_{SO}(r)$ which causes the fine-structure splitting must also be included as [95]

$$V_{SO}(r) = \frac{\alpha^2}{2r^3} \mathbf{L} \cdot \mathbf{S}, \quad (2.9)$$

where α is the fine-structure constant and

$$\mathbf{L} \cdot \mathbf{S} = \frac{j(j+1) - \ell(\ell+1) - s(s+1)}{2}. \quad (2.10)$$

The total potential is thus $V(r) = V_c(r) + V_{SO}(r)$.

Numerical integration

Using this model potential, the radial wavefunctions can be calculated by numerically integrating the radial Schrödinger equation of eq. 2.6. This is simplified by performing a transformation to integrate the function $X(r) = R(r)r^{3/4}$ in terms of the scaled co-ordinate $x = \sqrt{r}$ [96]. This transformation converts eq. 2.6 to a form solved efficiently using the Numerov algorithm [97, 98], whilst using the coordinate x gives an approximately constant number of points across each period of oscillation in the wavefunction. It is necessary to truncate the range of integration as at short range the model becomes unphysical and diverges, whilst at long range the wavefunction decays to zero. Following ref. [99], the limits of integration are set to use an inner radius of $r_i = \sqrt[3]{\alpha_c}$, and an outer radius of $r_o = 2n(n + 15)$ which is much larger than the classical turning point of the wavefunction. To minimise errors introduced by the approximate model potential at short range, the integration is performed inwards, starting at r_o .

Figure 2.1 (a) shows the calculated wavefunctions of the $50S_{1/2}$ states for hydrogen and rubidium as a function of the scaled coordinate. Comparing the two wavefunctions, the rubidium wavefunction is shifted to shorter radius relative to the hydrogen wavefunction due to the increased binding energy from the interaction with the core. In (b) the electron probability density is plotted for the $nD_{5/2}$ states, illustrating the large orbital radii of the Rydberg states.

2.3 Dipole matrix elements

Transitions between atomic states primarily occur due to coupling with the electric dipole moment $\boldsymbol{\mu} = e\mathbf{r}$ of the valence electron, which is a factor of $(\alpha/2)^2$ stronger than the magnetic dipole coupling [100]. The strength of the coupling between states $|n\ell m_\ell\rangle$ and $|n'\ell' m'_\ell\rangle$ is given by the dipole

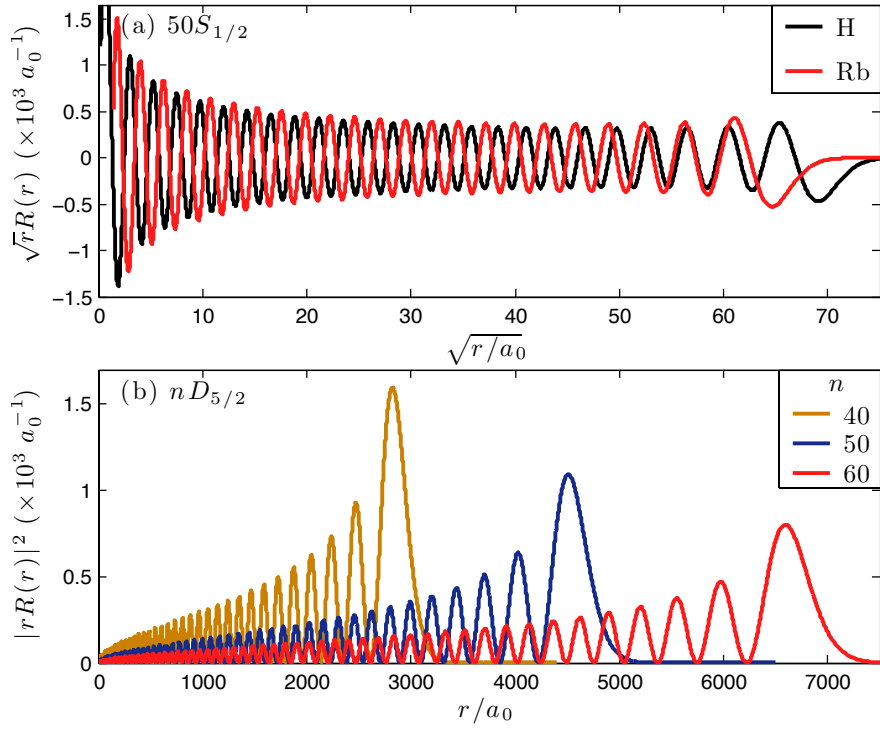


Figure 2.1: Rydberg atom radial wavefunctions. (a) $50S_{1/2}$ radial wavefunction for rubidium and hydrogen. (b) Radial probability density for $nD_{5/2}$ states, illustrating the scaling of the radial wavefunction with n^2 .

matrix element $\langle n\ell m_\ell | \mu | n'\ell' m'_\ell \rangle$, which is dependent upon the overlap of the wavefunctions with the electric dipole moment. From knowledge of the dipole matrix elements, it is possible to calculate transition probabilities, radiative lifetimes and many other properties of the atomic states [95].

The dipole operator is $\mu = e\mathbf{r} \cdot \hat{\mathbf{e}}$, where $\hat{\mathbf{e}}$ is the electric field polarisation unit vector. Transforming into the spherical basis, the dipole operator can be decomposed into the operators μ_q , with $q = \{-1, 0, +1\}$ corresponding to $\{\sigma^+, \pi, \sigma^-\}$ transitions, given by

$$\mu_{-1} = \frac{1}{\sqrt{2}}(\mu_x - i\mu_y), \quad (2.11a)$$

$$\mu_0 = \mu_z, \quad (2.11b)$$

$$\mu_{+1} = \frac{1}{\sqrt{2}}(\mu_x + i\mu_y). \quad (2.11c)$$

These operators are related to the spherical harmonics by $\mu_q = er\sqrt{4\pi/3}Y_1^q(\theta, \phi)$, which form a set of rank-1 irreducible tensors. As a result the Wigner-Eckart theorem can be used to separate dipole matrix element into an angular coupling and a reduced matrix element $\langle \ell || er || \ell' \rangle$ which depends only on ℓ and the radial wavefunctions [101]

$$\langle n\ell m_\ell | \mu_q | n'\ell' m'_\ell \rangle = (-1)^{\ell-m_\ell} \begin{pmatrix} \ell & 1 & \ell' \\ -m_\ell & q & m'_\ell \end{pmatrix} \langle \ell || \mu || \ell' \rangle, \quad (2.12)$$

where the brackets denote the Wigner-3j symbol. Using the properties of the Wigner-3j symbol, the selection rules of the electric dipole can be derived as $\Delta\ell = \pm 1$ and $\Delta m_\ell = 0, \pm 1$ corresponding to π, σ^\pm transitions.

The reduced matrix element is defined as [102]

$$\langle \ell || \mu || \ell' \rangle = (-1)^\ell \sqrt{(2\ell+1)(2\ell'+1)} \begin{pmatrix} \ell & 1 & \ell' \\ 0 & 0 & 0 \end{pmatrix} \langle n\ell | er | n'\ell' \rangle, \quad (2.13)$$

where the radial matrix elements $\langle n\ell | er | n'\ell' \rangle$ represent the overlap integral between the radial wavefunctions and the dipole moment

$$\langle n\ell | er | n'\ell' \rangle = \int_{r_i}^{r_o} R_{n,\ell}(r) er R_{n',\ell'}(r) r^2 dr, \quad (2.14)$$

This can be evaluated by numerical integration over the wavefunctions calculated using the method described above.

2.3.1 Fine structure basis

The fine structure interaction V_{SO} breaks the degeneracy of the ℓ states, which split according to $j = \ell + s$. As the electric field only couples to the orbital angular momentum (ℓ) of the electron, it is therefore necessary to transform from the fine-structure basis into the uncoupled basis to evaluate the dipole matrix elements. Using the Wigner-Eckart theorem (eq. 2.12),

the matrix element can be expressed in terms of the reduced matrix element $\langle j||\mu||j'\rangle$. This is related to $\langle \ell||\mu||\ell'\rangle$ by [101]

$$\langle j||\mu||j'\rangle = (-1)^{\ell+s+j'+1} \delta_{s,s'} \sqrt{(2j+1)(2j'+1)} \left\{ \begin{matrix} j & 1 & j' \\ \ell' & s & \ell \end{matrix} \right\} \langle \ell||\mu||\ell'\rangle, \quad (2.15)$$

where the braces denote a Wigner-6j symbol. Combining these equations, the dipole matrix element in the fine-structure basis is

$$\begin{aligned} \langle n\ell j m_j | \mu_q | n'\ell' j' m'_j \rangle &= (-1)^{j-m_j+s+j'+1} \sqrt{(2j+1)(2j'+1)(2\ell+1)(2\ell'+1)} \\ &\times \left\{ \begin{matrix} j & 1 & j' \\ \ell' & s & \ell \end{matrix} \right\} \begin{pmatrix} j & 1 & j' \\ -m_j & q & m'_j \end{pmatrix} \begin{pmatrix} \ell & 1 & \ell' \\ 0 & 0 & 0 \end{pmatrix} \langle n\ell j' | er | n'\ell' j' \rangle. \end{aligned} \quad (2.16)$$

2.3.2 Hyperfine structure basis

The hyperfine interaction couples the angular momentum of the electron (j) and the nucleus (I), further lifting the degeneracy of the states which are split according to the total angular momentum $F = j + I$. As with the fine-structure splitting, the Wigner-Eckart theorem can be used to find the matrix elements in the hyperfine basis in terms of the reduced matrix element $\langle F||\mu||F'\rangle$, which can similarly be reduced to $\langle j||\mu||j'\rangle$.

For the Rydberg states the hyperfine splitting is typically small compared to the interaction with external fields *e.g.* $\nu_{\text{hfs}} \simeq 200$ kHz at $n = 60S_{1/2}$ [92]. The hyperfine splitting can therefore be neglected, treating Rydberg atoms in the fine-structure basis.

2.3.3 Rydberg excitation transition strengths

In the experiments presented in this thesis, Rydberg states are excited by a two-photon transition in rubidium, using a laser at 780 nm to excite from the

$5S_{1/2}$ ground-state to the $5P_{3/2}$ excited state, and a second laser at 480 nm to couple from $5P_{3/2}$ to either $nS_{1/2}$ or $nD_{5/2,3/2}$ Rydberg states. The coupling strength can be expressed in terms of the Rabi frequency $\Omega = -\boldsymbol{\mu} \cdot \mathbf{E}/\hbar$, which scales linearly with the dipole matrix element. For experiments where the coupling Rabi frequency is to be kept constant over a range of n , it is necessary to calculate the dipole matrix elements for the transition. Using the core potential and the energy of the $5P_{3/2}$ state¹, an approximate $5P_{3/2}$ wavefunction can be calculated to find the radial dipole matrix elements $\langle 5P_{3/2} | er | n\ell j \rangle$ for the allowed transitions. The results are plotted in fig. 2.2, showing a stronger coupling to the $nD_{5/2}$ state. The matrix elements are around 5 orders of magnitude weaker than the coupling to the nearest Rydberg states ($\sim 1000 \text{ } ea_0$ at $n=40$), and are fitted using the scaling $C_\ell n^{*-3/2}$ to obtain the coefficients $C_S = 4.502 \text{ } ea_0$ and $C_D = 8.457 \text{ } ea_0$, in good agreement with Deiglmayr *et al.* [47].

The total matrix element is obtained by multiplying the radial part by the angular component. For transition between the stretched states with $j =$

¹ Below $n \sim 20$ the quantum defects give poor agreement as the electron has a strong interaction with the core.

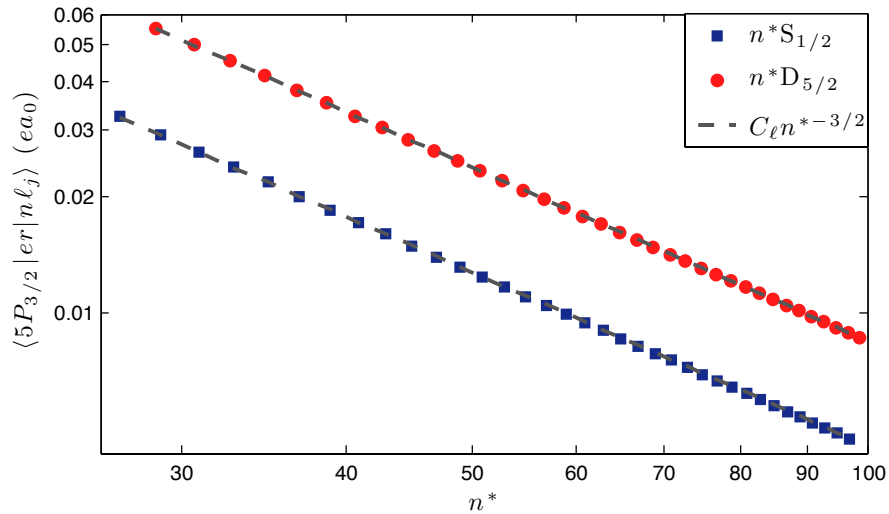


Figure 2.2: Radial matrix elements for $5P_{3/2}$ to $nS_{1/2}$ or $nD_{5/2}$ transitions. The matrix elements scale as $n^{*-3/2}$.

$\ell + 1/2$, $|m_j| = j$, the angular coupling of eq. 2.16 reduces to

$$\langle P_{3/2}, m_j = 3/2 | \mu_q | \ell' j' m'_j \rangle = \sqrt{\frac{\ell_{\max}}{(2\ell_{\max} + 1)}}, \quad (2.17)$$

giving $\sqrt{1/3}$ for transitions to $nS_{1/2}, m_j = 1/2$ and $\sqrt{2/5}$ to $nD_{5/2}, m_j = 5/2$, further enhancing the coupling to $nD_{5/2}$ relative to $nS_{1/2}$.

2.4 Stark shift

Applying a static electric field E along the z -axis causes the states to mix, shifting the energy levels relative to the bare atom, known as the Stark shift. To calculate the atomic energy states in the presence of an electric field, it is necessary to find the eigenvalues of the Stark Hamiltonian [99]

$$\mathcal{H}_{\text{Stark}} = \mathcal{H}_{\text{atom}} + E\hat{z}. \quad (2.18)$$

The electric field term $E\hat{z}$ creates off-diagonal couplings between states, with the selection rule $\Delta m_j = 0$ such that $|m_j|$ states are coupled together. The new energy levels are found by diagonalising $\mathcal{H}_{\text{Stark}}$ as a function of E for all states with a given $|m_j|$ to create an energy diagram known as a Stark map.

Figure 2.3 shows Stark maps calculated at $n = 40$ for the $|m_j| = 1/2$ and $5/2$ manifolds. The angular momentum states are truncated at $\ell = 20$ as this is sufficient for convergence of the energy levels of the states for $\ell \leq 3$. From (a), the effect of the quantum defects in shifting the energy levels is clear, as the closest $S_{1/2}$ state to the $n = 40$ hydrogenic manifold is $43S_{1/2}$. The high- ℓ hydrogenic states are degenerate, leading to a first-order linear Stark shift. In the $|m_j| = 1/2$ states, all of the levels are coupled leading to avoided crossings between the states with closest ℓ . In (b), the $|m_j| = 5/2$ hydrogenic states separate into $|m_\ell| = 2, 3$ states. This is the relevant quantum number as the electric field couples to ℓ , leading to a mixture of real and avoided

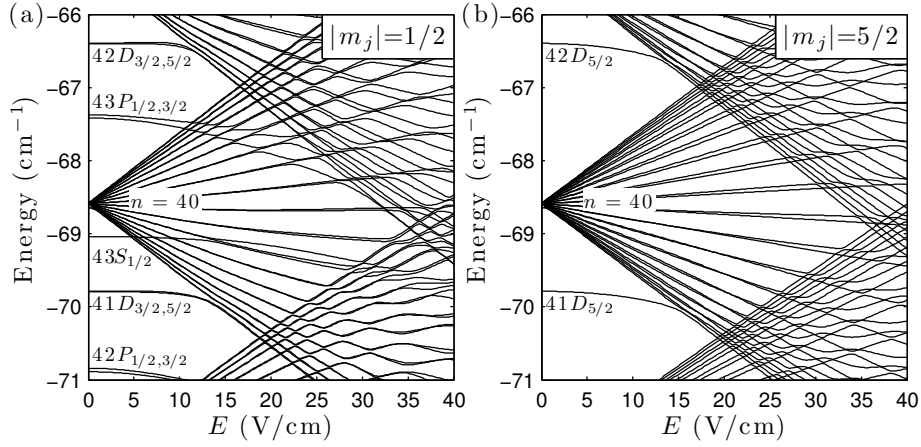


Figure 2.3: $n = 40$ Stark maps for Rb. (a) $|m_j| = 1/2$ manifold shows avoided crossings between states with $\Delta\ell = \pm 1$. (b) $|m_j| = 5/2$. Hydrogenic states are split into $|m_\ell| = 2, 3$ manifolds, resulting in a mixture of avoided and real crossings between adjacent n states.

crossings observable between adjacent n states.

2.4.1 Scalar polarisability

At low fields, the Stark effect acts as a second-order perturbation on the states with $\ell \leq 3$ to give a quadratic shift of the form

$$\Delta W = -\frac{1}{2}\alpha_0 E^2, \quad (2.19)$$

where α_0 is the static polarisability, which for state $|n, \ell, j, m_j\rangle$ is given by

$$\alpha_0 = \sum_{n', \ell', j' \neq n, \ell, j} \frac{|\langle n, \ell, j, m_j | \mu_0 | n', \ell', j', m_j \rangle|^2}{W_{n' \ell' j'} - W_{n \ell j}}. \quad (2.20)$$

The polarisability $\alpha_0 \simeq \mu^2/\Delta$, where $\Delta \propto n^{*-3}$ is the energy of the nearest state and $\mu \propto n^{*2}$, giving $\alpha_0 \propto n^{*7}$. Consequently Rydberg states are incredibly sensitive to electric fields, allowing precise control over the Rydberg energy levels and making them suitable for applications in electrometry [83, 103, 104].

The static polarisabilities can be obtained experimentally by fitting the low-field dependence of the energy-levels for each state. To test the accuracy of the code, the polarisabilities calculated from eq. 2.20 for the $nS_{1/2}$ states are compared to the measurements of O’Sullivan *et al.* [105]. The results are plotted in fig. 2.4 (a), showing excellent agreement between theory and experiment. In [105] the authors fit the data to an empirical scaling of the form

$$\alpha_0 = \beta_1 n^{*6} + \beta_2 n^{*7}, \quad (2.21)$$

where α_0 is in units of $\text{MHz}/(\text{V}/\text{cm})^2$, obtaining $\beta_1 = 2.202 \times 10^{-9}$ and $\beta_2 = 5.53 \times 10^{-11}$ for the measured data. Table 2.2 shows the results obtained from least-square fitting this scaling to the calculated polarisabilities over the range $n=20$ – 100 for all states with $\ell \leq 3$, which are consistent these empirical values for the $nS_{1/2}$ states. For $|m_j| = 1/2$ in the D states, the static polarisability is initially positive at low n and changes sign to become negative for the higher excited states, shown in fig. 2.4 (b). This gives a positive Stark shift at low field for states above $24D_{5/2}$. However, as the electric field increases, the D -states have an avoided crossing with the F -states and the energy shift becomes negative again. This can be seen from the Stark map in fig. 2.3 (a).

State	$ m_j $	$\beta_1 (\times 10^{-9})$	$\beta_2 (\times 10^{-11})$	State	$ m_j $	$\beta_1 (\times 10^{-9})$	$\beta_2 (\times 10^{-8})$
$S_{1/2}$	1/2	2.188	5.486	$F_{1/2}$	1/2	-1.655	1.612
$P_{1/2}$	1/2	2.039	51.456	$F_{1/2}$	3/2	-1.308	1.350
$P_{3/2}$	1/2	2.449	62.011	$F_{1/2}$	5/2	-0.634	0.826
$P_{3/2}$	3/2	1.611	52.948	$F_{1/2}$	1/2	-1.624	1.623
$D_{3/2}$	1/2	2.694	-6.159	$F_{1/2}$	3/2	-1.457	1.478
$D_{3/2}$	3/2	1.725	22.259	$F_{1/2}$	5/2	-1.077	1.188
$D_{5/2}$	1/2	2.770	-12.223	$F_{1/2}$	7/2	-0.530	0.753
$D_{5/2}$	3/2	2.352	1.772				
$D_{5/2}$	5/2	1.513	29.763				

Table 2.2: Parameters for calculating static polarisability $\alpha_0 = \beta_1 n^{*6} + \beta_2 n^{*7}$ in units of $\text{MHz}/(\text{V}/\text{cm})^2$.

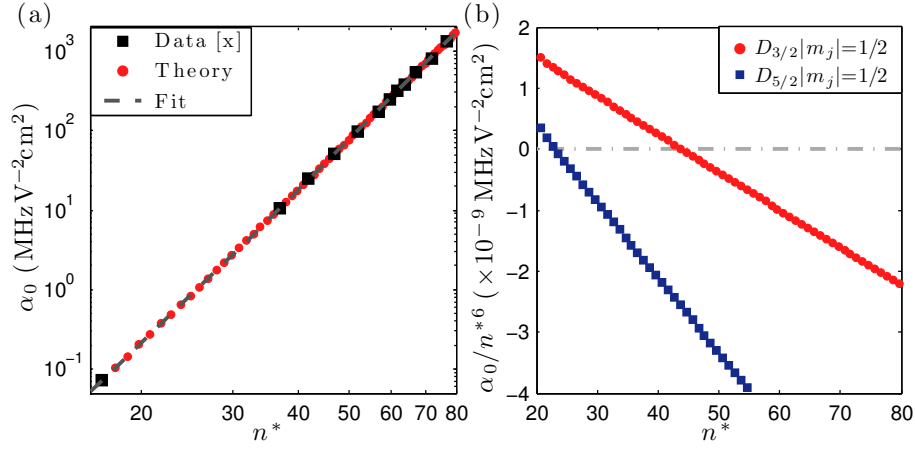


Figure 2.4: Scalar polarisability. (a) Comparison of calculated $nS_{1/2}$ static polarisabilities α_0 to experimental data from ref. [105]. (b) The static polarisability for the $D_{5/2,3/2} |m_j|=1/2$ states changes sign, resulting in a blue-shift at low fields.

2.5 Summary

The Rydberg series describes a set of states with simple scaling laws for fundamental properties such as transition frequencies, radiative lifetime or static polarisability in terms of the principal quantum number, which can be derived from the analytic solutions for the wavefunctions of hydrogen. For the alkali metal atoms, the interaction with the core creates a perturbation to the hydrogenic states that is characterised by the quantum defects. Using a model potential, the wavefunctions can be obtained numerically, enabling calculation of the transition dipole matrix elements between the states. From these matrix elements a wide range of properties can be calculated, such as the electric field sensitivity as described above. The most important property of the Rydberg states is the large dipole moment for transitions to adjacent Rydberg states $\propto n^{*2}$. As will be shown in the following chapter, this leads to very strong interactions between a pair of atoms excited to the Rydberg state.